Computational Particle Mechanics (2024) 11:1851–1862
https://doi.org/10.1007/s40571-024-00789-w

Modeling and mitigation of vortex formation in ejector deep hole drilling with smoothed particle hydrodynamics

Andreas Baumann[1] · Julian Frederic Gerken[2] · Daniel Sollich[1] · Nuwan Rupasinghe[1] · Dirk Biermann[2] · Peter Eberhard[1]

Received: 23 February 2024 / Revised: 14 May 2024 / Accepted: 6 June 2024 / Published online: 3 July 2024

Abstract

Ejector deep hole drilling achieves high-quality boreholes in production processes. High feed rates are applied to ensure a high productivity level, requiring reliable chip removal from the cutting zone for a stable process. Therefore, a constant metalworking fluid flow under high volume flow rates or high pressure is required. Experimental results show a vortex formation at the outer cutting edge. This vortex can lead to delayed chip removal from the cutting zone, and ultimately, it can lead to chip clogging and result in drill breakage due to increased torque. This paper investigates modified drill head designs using the smoothed particle hydrodynamics method. The investigated modifications include various designs of the chip mouth covering. Besides graphical analysis based on flow visualizations, flow meters are placed at the tool's head to evaluate the impact of the modifications on the flow rate and possible increased resistance and relocation of the fluid flow from the outer cutting edge to other parts of the tool. The simulation results for the reference design show the experimentally observed vortex formation, validating the simulation model. By adding the tool's rotation in the SPH simulation, which is not included in the experiments for observation reasons, the vortex formation is positively influenced. In addition, some designs show promising results to further mitigate the vortex formation while maintaining a sufficient fluid flow around the cutting edges.

Keywords Ejector deep hole drilling · Tool modification · Smoothed particle hydrodynamics (SPH) · Cutting tool

1 Introduction

Deep hole drilling (DHD) processes are characterized by machining high-quality boreholes with a length-to-diameter ratio larger than 10. Their applications are in various fields, such as automotive, aerospace or medical industries and are used to manufacture hydraulic cylinders, gear shafts or valve guides in marine fuel engines. Different DHD methods are available, ranging from diameters less than one millimeter up to 1500 mm. The classical DHD methods are single-lip drilling, drilling with a single-tube (BTA drilling) or double-tube system (ejector drilling). All methods are characterized by the high demands, e.g. in terms of roundness, diameter accuracy and surface quality, and the high level of productivity that is achieved. In addition, DHD at high feed rates ensures high cutting performance; thus, the chip and metalworking fluid removal from the cutting zone is essential for a stable process. This can be achieved by a constant metalworking fluid (MWF) flow under high volume flow rates or high pressure.

In contrast to single-lip and twist DHD, the chips are removed through the inside of the tool during ejector drilling. Thus, the chips have no contact to the bore hole wall, which improves the surface quality. A further advantage is that there is no need for a high-pressure sealing between the face of the workpiece and the drill bush. As a result, the ejector method makes the benefits of DHD, such as high material removal rates and high hole quality, available to industry on conventional machining centers by eliminating the need for an expensive DHD machine [6]. Figure 1 shows the schematic tool design, the detailed view of the MWF supply and the separation of the flow paths.

✉ Peter Eberhard
peter.eberhard@itm.uni-stuttgart.de

1 Institute of Engineering and Computational Mechanics, University of Stuttgart, Pfaffenwaldring 9, 70569 Stuttgart, Germany

2 Institute of Machining Technology, TU Dortmund University, Baroper Str. 303, 44227 Dortmund, Germany

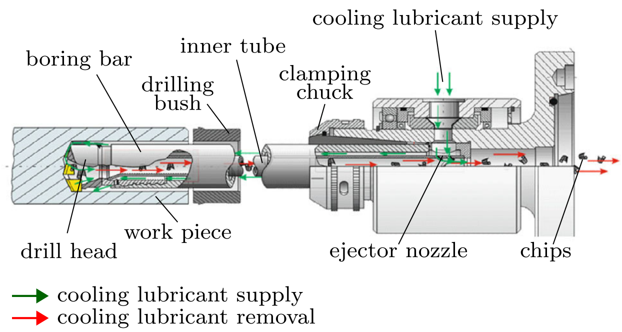

Fig. 1 Process principle and structure of an ejector DHD system

One part of the MWF supply is realized through an annular gap between the inner tube and the boring bar. The MWF emerges through bores at the drill head, flows around the cutting edge area and flushes away the chips through the inner tube. The inner tube has slits in the area of the feed system, which are known as ejector nozzles. The second part of the MWF is guided through the ejector nozzles into the inner tube and then straight out of the system. This particular MWF guidance causes a negative pressure in the inner pipe based on the Venturi principle, which is known as the ejector effect. This supports the chip removal and prevents MWF leakage on the outside of the tool [6]. An additional drilling bush is used for stabilization and to center the drill at the start of the drilling process.

Earlier investigations already found an influence of the ejector design on the chip removal conditions [3]. The required hydraulic energy is highly influenced by the positioning and the geometric shape of the ejector nozzle, whereas the operating head seemed to have no influence on the hydraulic efficiency thus the chip removal. However, high-speed recordings and visualizations of the flow lines using particle image velocimetry show the formation of a vortex at the outer cutting edge [11]. This vortex can lead to a delayed chip removal from the cutting zone as small chips can be caught in the vortex. In consequence, the removal of chips is slower than they are produced. This can lead to chip clogging and results in drill breakage due to an increased torque [16].

Several investigations have looked into calculating drilling forces and torques required to evacuate chips during the drilling process [10, 19, 20]. Based on threshold values, a pecking cycle (periodic drill retraction) or cutting parameter changes are applied. Other approaches are based on in-process prediction, monitoring or controllers to optimize the machined chip form [12, 26]. Both approaches aim to prevent drill breakage through in-process actions.

Instabilities of the coolant supply in the annular coolant channels of BTA drilling are observed in [2]. Theses instabilities are explained by vortices in the inlet annular channels, which occur under certain combinations of drill rotational velocity and axial flow velocity. Further works [8] studied the influence of the fluid flow on the shaft behavior for BTA drilling. However, the flow behavior in BTA drilling cannot be transferred to ejector drilling, as for BTA drilling higher inflow pressures are applied and a fully flooded bore hole occurs, which results in no occurrence of a MWF and air mixture at the cutting head [6]. The high pressure and the consequently high flow velocities at the cutting edges in BTA drilling avoid the possibility of chip clogging [32].

The methods applied in this paper have been applied for single-lip deep hole drilling by the authors to investigate the dynamic evacuation of chips for different single-lip drill designs. Digitized chip forms from experiments were used in a dynamic smoothed particle hydrodynamics (SPH) simulation. It was shown that the drill design changes and the thereby changing chip forms influence the evacuation speed of the chips [27, 28].

SPH is a method for the description of fluids by discrete moving interpolation points, the so-called particles. Therefore, the Navier–Stokes equations describing the fluid movement are represented by weighted sums over a set of neighbor particles [35]. Its Lagrangian and mesh-free nature allows SPH to describe arbitrary moving surfaces and interfaces. Its areas of application are especially when non-regular, moving free surfaces or dynamic fluid/structure interaction are present. SPH has been applied in the investigation of the chip evacuation of twisted deep hole drills [4], the fluid distribution and design changes in single-lip drills [5], or even the modeling of complex laser welding with changing phases and a moving liquid melt [34]. SPH is explained in Sect. 3 in more detail.

The novel contribution of this paper is the simulation-based investigation of different variants of improved drill head concepts and their influence on the fluid flow. Therefore, in Sect. 2 the experimental setup to observe the problematic vortex is presented, and in Sect. 3, the modeling for the simulation-based investigation is shown. The simulations results are given in Sect. 4, and the resulting conclusions are presented in Sect. 5.

2 Experimental investigation

In order to fully analyze and improve deep hole drilling processes and tools, it is essential to gain fundamental knowledge of the chip formation processes and flow characteristics in the cutting zone. As there is no optical access to the cutting zone during drilling, unlike other machining processes with geometrically defined cutting edges, such as milling or turning, a reference test rig is developed for the optical analysis of flow characteristics and chip formation with a modified coolant circuit, as shown schematically in Fig. 2.

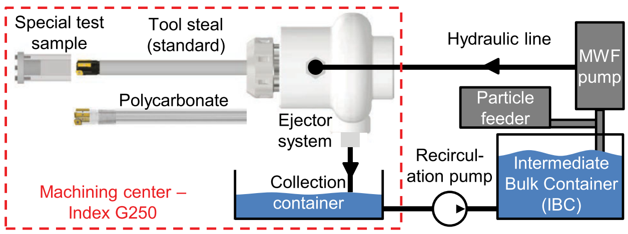

Fig. 2 Experimental test rig for the optical analysis

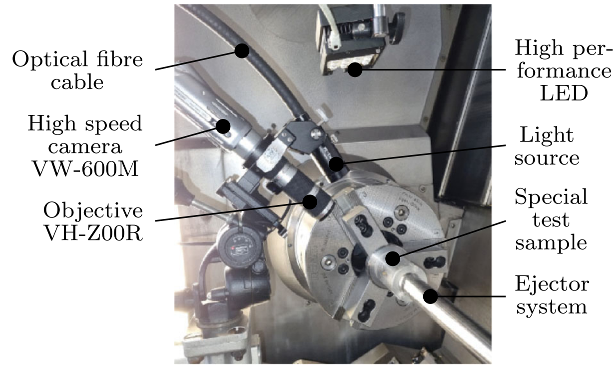

Fig. 3 Camera setup for the optical analysis

As a result of the asymmetric design of the drill head, it is necessary to support the screwed-on guide pads on the bore wall as they guide the tool in the bore and result in self-centering. Therefore, removal of the bore wall is not easily possible and a special test specimen had to be developed. Due to the high opacity of the emulsion used, the experiments are carried out with water. For this purpose, the external coolant immersion pump is adapted to a water tank. The water/chip mixture exiting the ejector system is directed into a collection container where the chips are separated by a grid and the water is circulated back into the water tank by a recirculation pump. A customized tooling system (ejector drill head, boring bar and inner tube) made of highly transparent polycarbonate is used to analyze the flow characteristics at the drill head and inside the double-tube system. The flow is visualized by polyamide particles in the water with a diameter of $d = 100\,\mu\text{m}$, so that they are large enough to be captured optically by the high-speed camera without affecting the flow. By manually comparing the polyamide loaded water flow with the metalworking fluid flow without particles, the quantitative flow patterns and characteristics are identical. General flow patterns such as the vortex formation at the cutting edge or larger features at the surface can be seen for the opaque MWF emulsion too. For detailed insights in deeper layers and fluid velocities, the PIV is needed. This approach was discussed with other researchers and is documented in [11]. In addition, a stable deep drilling process with an ejector effect can be achieved with the use of polyamide particles. The polyamide particles are fed directly into the suction area of the submersible pump using a compact aquarium pump. This makes it possible to capture the particles with repeatable accuracy using a high-speed camera. Due to the ejector effect, air may be temporarily sucked in from the machine room, causing air bubbles to be injected into the flow and causing local opacities. This can be prevented by adjusting the flow rate of the MWF pump and must be done before starting the optical measurements The modular camera configuration includes a main unit, a high-speed camera and a close-up lens to visually record the flow characteristics and chip formation, which can be seen in Fig. 3. Combined with an adapted high-speed monochrome camera, 4000 frames per second can be captured at a resolution of 640 × 480 pixels. The frame rate can be increased to 230,000 frames per second with a significant reduction in image resolution (160 × 32 pixels). In field tests, 4000 fps are recorded at a resolution of 640 × 480 pixels. The high-speed camera is equipped with a VH Z00R macro zoom lens. This lens focuses at a distance of AD = 95 mm and enlarges the recording area by a factor of 5–50. Field tests are recorded at 5× magnification. The lens is equipped with a VW-L1 illumination unit. The illumination unit is connected to the main unit via an optical fiber cable. An additional MultiLED QT light source is used in parallel to improve the brightness dynamics. It is attached to the milling spindle of the machining center using a magnetic stand and provides 12,000 lumen.

Digital analysis methods are used to track the polyamide particles and make quantitative statements about flow characteristics and velocity. This is achieved through automated image analysis using the PIVlab—particle image velocimetry graphical user interface of the MATLAB software. Compared to manual analysis, digital image analysis has a major advantage in being quantitative and time-efficient. This is because the paths of the individual particles do not have to be tracked frame by frame. Furthermore, it is not necessary to manually measure the distances traveled by the particles. The software's implicit particle tracking algorithm uploads the individual images of the recordings and runs them through a loop. The steps for flow analysis are divided into import, image preprocessing, calculation and analysis, post-processing, and final data acquisition. During the post-processing flow analysis step, the local displacement vectors of individual image pairs are plotted and checked for anomalies. To validate the results, the vectors are displayed in scatter plots, and statistically unlikely particles with strongly deviating directions and velocities are removed using a predefined boundary frame. For the final output, the vectors of the image pairs are averaged for the analyzed time period and plotted in a vector field as a velocity profile. In the evaluation, two consecutive images are compared [30]. The images are divided into smaller regions of interest. Using auto- or cross-correlation, the displacement of a particle in the known time interval and thus its local velocity vector

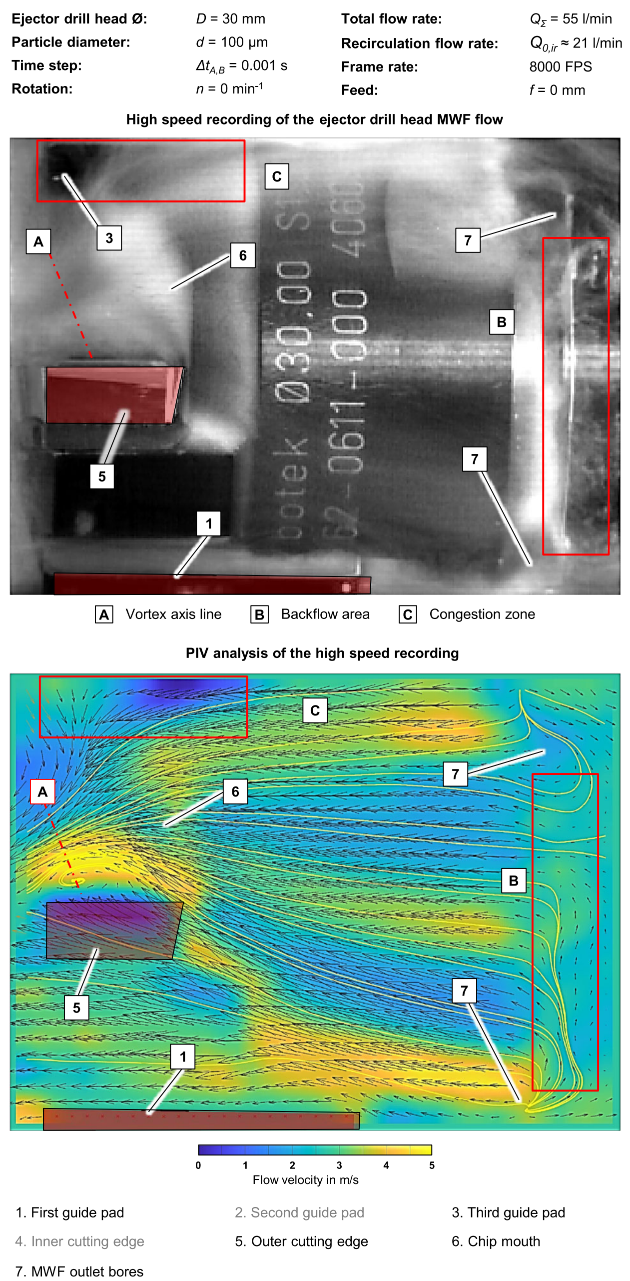

Fig. 4 Visualization of the MWF flow lines in the drill head area during ejector deep hole drilling and the automated evaluation with PIVlab

can be determined. Three local flow characteristics can be identified using particle image velocimetry analysis, labeled (A)–(C) in Fig. 4. One characteristic feature is the formation of a flow vortex (A) with an axis of rotation located above the outer cutting edge. This is caused by the velocity difference of the opposing flow directions resulting from the deflection of the recirculation volume flow in the area of the bore bottom due to the ejector effect. In area (B), after leaving the MWF outlet bores, there is a return flow area of the MWF in the opposite direction to the feed direction. This is caused by the design of the MWF outlet bores. With the standard drill head, the MWF exits the drill head as a free jet at a 90° angle and is passed directly to the overhang of the drill rod as an impingement flow. A congestion zone with a significantly reduced flow velocity can be identified in the contact area of the third guide pad (C). The analysis suggests that a design adaptation utilizing a drain from the contact area to the chip mouth has great potential for improvement. This adaptation directs the lubricant flow specifically to the contact/cutting area, increasing the flow velocity v_{KSS} and avoiding the occurrence of stagnation zones. The additional lubrication improves the achievable bore quality.

The particle image velocimetry analysis of the cutting head shows that the highest flow velocities are up to $v_{\mathrm{KSS}} \approx 5\,\mathrm{m} \cdot \mathrm{s}^{-1}$ as shown in Fig. 4. The turbulent flow in the area (B) has been investigated in [14]. Different variations of the MWF outlet bores were compared using numerical models to reduce the turbulent vortices caused by the outlet bores. These design adaptations are not explicitly considered in this investigation, which focuses on design modifications of the chip mouth. However, the results achieved by [14] create a laminar flow through the outlet bores. Therefore, the simulation model applied in this investigation applies an already laminar inflow after the MWF outlet bores. The previous investigation of the ejector drill showed the significant potential of SPH simulations for analyzing the impact of structural changes to drill head design, as they eliminate the need for expensive prototype production. In the following, SPH will also be applied to analyze modifications of the chip mouth design.

3 Modeling and geometric design

The simulation model of the ejector drill head is based on the smoothed particle hydrodynamics method. In the following, first the simulation method is explained, and afterward, the simulation model itself, its boundary conditions and the investigated drill designs are described.

3.1 Smoothed particle hydrodynamics

SPH is a meshless Lagrangian method where the continuum medium is discretized by a collection of points called particles. In order to compute the physical attributes of fluid flow problems, SPH solves the Navier–Stokes (N–S) equations using these points. Its mesh-free nature allows SPH to model changing surfaces and interfaces easily. This makes SPH advantageous in problems like the modeling of ejector deep hole drilling, as the fluid domain is constantly evolving, which may be computationally expensive to track using conventional mesh-based methods.

Two steps are necessary to obtain an SPH formulation: the *kernel approximation*, where a function and/or its derivatives are represented in integral form, and the *particle approximation*, which describes the discretization using a collection of moving particles for the computational domain [17, 35]. First, we start from an identity,

$$A(\mathbf{x}) = \int_{\mathbf{x}' \in \Omega} A(\mathbf{x}')\delta(\mathbf{x} - \mathbf{x}')d\Omega, \tag{1}$$

where $A(\mathbf{x})$ is a function which needs to be approximated, $\mathbf{x}$ is a position vector and Ω is the complete domain that contains $\mathbf{x}$. The Dirac delta distribution $\delta(\mathbf{x} - \mathbf{x}')$ is given by

$$\delta(\mathbf{x} - \mathbf{x}') = \begin{cases} \infty & \text{for } \mathbf{x} = \mathbf{x}', \\ 0 & \text{else.} \end{cases} \tag{2}$$

The Dirac delta distribution $\delta(\mathbf{x} - \mathbf{x}')$ is then replaced by the smoothing kernel function $W(\mathbf{x} - \mathbf{x}', h)$, where h is the smoothing length. Finally, the kernel approximation for $A(\mathbf{x})$ is obtained via

$$A(\mathbf{x}) \approx \langle A(\mathbf{x}) \rangle = \int_{\mathbf{x}' \in \Omega} A(\mathbf{x}')W(\mathbf{x} - \mathbf{x}', h)d\Omega. \tag{3}$$

The kernel function $W(\mathbf{x} - \mathbf{x}', h)$ can be selected by the user. However, it must obey certain conditions [17, 33]. For the following simulations, the fifth degree Wendland kernel function is used [36]. Hereafter, the integral form of the kernel approximation is descretized by weighted summation of a finite set of neighboring particles, providing the particle approximation

$$\langle A(\mathbf{x}) \rangle = \sum_b \frac{m_b}{\rho_b} A_b W(\mathbf{x} - \mathbf{x}_b, h). \tag{4}$$

Due to its compact support, the summation is localized to the effective neighboring particles b known as the *support domain* defined by h of the smoothing function instead of the entire particle set. Each particle carries a mass m and density ρ. Therefore, the corresponding volume assigned to particle b is given by $\frac{m_b}{\rho_b} = d\Omega_b$. SPH can be used to approximate the solution of arbitrary partial differential equations, like the Navier–Stokes equations, which describe the motion of fluids. Therefore, the continuity equation, kinematics equation and the equation of state are introduced next.

The Navier–Stokes equations provide a general description for all kinds of flows in fluid dynamics. Traditionally, the N–S equations are derived by applying the balance of linear momentum for an infinitesimal volume of fluid with many different forces considered. In Lagrangian form, they are written as

$$\rho \frac{\mathrm{d}\mathbf{v}}{\mathrm{d}t} = \rho \left(\frac{\partial \mathbf{v}}{\partial t} + (\mathbf{v} \cdot \nabla)\mathbf{v} \right) = \rho \mathbf{g} - \nabla p + \mu \nabla^2 \mathbf{v}, \tag{5}$$

where $\mathbf{v}$ is velocity, t is time, $\mathbf{g}$ is gravity, p is pressure and μ is the dynamic viscosity [18]. The N–S equations are complemented by a statement of conservation of mass through the continuity equation,

$$\frac{\mathrm{d}\rho}{\mathrm{d}t} = -\rho \nabla \cdot \mathbf{v}, \tag{6}$$

and the relation between position $\mathbf{r}$ and velocity $\mathbf{v}$ from a kinematic equation,

$$\frac{\mathrm{d}\mathbf{r}}{\mathrm{d}t} = \mathbf{v}. \tag{7}$$

A relation between density and pressure provided by the equation of state ensures that the same number of equations for the unknowns ρ, $\mathbf{v}$, p, $\mathbf{r}$ are available. For SPH, the *Tait* equation is commonly used as the equation of state [9], which is given by

$$p = \frac{c_0^2 \rho_o}{\gamma} \left[\left(\frac{\rho}{\rho_o} \right)^{\gamma} - 1 \right]. \tag{8}$$

Here, c_0 denotes the numerical speed of sound, ρ_o is a reference density, and the polytropic index is represented by γ. In general, this equation of state is quite stiff, requiring small step sizes during the numerical integration. This approach is commonly referred to as weakly compressible SPH (WCSPH) formulation due to the choice of a numerical speed of sound c_0 lower than the actual speed of sound of the fluid. In WCSPH, the numerical speed of sound c_0 is chosen as ten times the maximum velocity expected in the fluid flow. This provides a reasonable time step size during numerical integration while the density fluctuations remain less than 1% [35]. Usually, γ is set to 7 for water [21].

Equations 5 and 6 are solved at discrete particle positions in the SPH environment. The N–S equation in discretized SPH form is given by

$$\left.\frac{\mathrm{d}\mathbf{v}}{\mathrm{d}t}\right|_a = \mathbf{g} - \sum_b m_b \left[\left(\frac{p_a}{\rho_a^2} + \frac{p_b}{\rho_b^2} \right) - \frac{1}{\rho_a \rho_b} \frac{(\mu_a + \mu_b)\mathbf{v}_{ab} \cdot \mathbf{n}_{ab}}{||\mathbf{n}_{ab}||^2 + 0.01h^2} \right] \nabla_a W_{ab}, \tag{9}$$

and the continuity equation reads

$$\left.\frac{\mathrm{d}\rho}{\mathrm{d}t}\right|_a = \rho_a \sum_b \frac{m_b}{\rho_b} (\mathbf{v}_a - \mathbf{v}_b) \cdot \nabla_a W_{ab}, \tag{10}$$

where W_{ab} denotes the kernel function $W(\mathbf{x}_a - \mathbf{x}_b, h)$ in its simplified notation and ∇_a describes the partial derivative at a particle a and its position. Further details about the SPH method are provided in [17, 35].

For the temporal discretization of the previously provided balance Eqs. (7), (10) and (9), a predictor–corrector leapfrog scheme is applied [23]. To improve the readability, Eqs. (10) and (9) are abbreviated by

$$\frac{\mathrm{d}\mathbf{v}}{\mathrm{d}t} = \mathbf{F} \quad \text{and} \tag{11}$$
$$\frac{\mathrm{d}\rho}{dt} = D. \tag{12}$$

The values of the variables at the beginning of a time step is denoted by $\mathbf{r}^0$, $\mathbf{v}^0$, $\mathbf{F}^0$, ρ^0 and D^0, and the time step is given by Δt. The predictor step reads

$$\mathbf{r} = \mathbf{r}^0 + \Delta t \mathbf{v}^0 + \frac{1}{2}(\Delta t)^2 \mathbf{F}^0, \tag{13}$$
$$\mathbf{v}_p = \mathbf{v}^0 + \Delta t \mathbf{F}^0, \quad \text{and} \tag{14}$$
$$\rho_p = \rho^0 + \Delta t D^0. \tag{15}$$

The value for $\mathbf{r}$ is not corrected as its prediction is already of a higher order than for the other variables [25]. Based on the predicted quantities from Eqs. (13), (14) and (15), new values of $\mathbf{F}$ and D are calculated. Then, corrected values of $\mathbf{v}$ and ρ are calculated according to

$$\mathbf{v} = \mathbf{v}_p + \frac{1}{2}\Delta t \left(\mathbf{F}_p - \mathbf{F}^0\right), \quad \text{and} \tag{16}$$
$$\rho = \rho_p + \frac{1}{2}\Delta t \left(D_p - D^0\right). \tag{17}$$

The applied time step Δt is limited by

$$t = C_{\mathrm{CFL}} \min \begin{pmatrix} \min\left(\frac{h}{||\mathbf{v}_i||}\right) \\ \min\left(\sqrt{\frac{h}{||\mathbf{F}_i||}}\right) \\ \frac{h}{c_0} \\ \frac{h^2}{\mu} \end{pmatrix} \tag{18}$$

where C_{CFL} is the Courant–Friedrichs–Levy safety constant and the index i runs over all particles.

Due to the nature of the implementation of the kernel function, SPH approximations suffer from inconsistencies near open free surfaces due to incomplete kernel support. Corrected kernels and corrected gradients for boundaries are used to treat these errors rising from incomplete kernel support and disordered particle distributions. Kernel gradient correction is a simple and efficient approach implemented to improve the numerical accuracy and the consistency of the simulation. Therefore, the kernel gradient is replaced by the modified version [7]

$$\widetilde{\nabla}_a W_{ab} = \widetilde{\boldsymbol{L}}_a \nabla_a W_{ab} \tag{19}$$

where the correction matrix $\widetilde{\boldsymbol{L}}_a$ is given by

$$\widetilde{\boldsymbol{L}}_a = \left(\sum_b \frac{m_b}{\rho_b} \nabla_a W_{ab} \otimes (\boldsymbol{x}_b - \boldsymbol{x}_a)\right)^{-1}. \tag{20}$$

Additionally, one of the drawbacks of the standard WCSPH is having spurious numerical oscillations in the pressure field since its evaluation is based on density variations. This is mitigated in the δ-SPH approach presented in [1] by adding an artificial diffusion term to the continuity equation to remove these high-frequency oscillations,

$$\left.\frac{\mathrm{d}\rho}{\mathrm{d}t}\right|_a = \sum_b m_b \frac{\rho_a}{\rho_b}(\mathbf{v}_a - \mathbf{v}_b) \cdot \nabla W_{ab} + \delta h c_0 \sum_b \frac{m_b}{\rho_b} \boldsymbol{\psi}_{ab} \cdot \nabla W_{ab}, \tag{21}$$

in which the parameter δ is used to control the diffusion behavior of density. The vector $\boldsymbol{\psi}_{ab}$ is defined as

$$\boldsymbol{\psi}_{ab} = 2(\rho_b - \rho_a)\frac{\mathbf{x}_b - \mathbf{x}_a}{||\mathbf{x}_a - \mathbf{x}_b||^2} - \left(\langle\nabla\rho\rangle_a^L + \langle\nabla\rho\rangle_b^L\right), \tag{22}$$

where the re-normalized density gradient takes the form

$$\langle\nabla\rho\rangle_a^L = \sum_b \frac{m_b}{\rho_b}(\rho_b - \rho_a)\widetilde{\boldsymbol{L}}_a \nabla W_{ab} \tag{23}$$

and $\widetilde{\boldsymbol{L}}_a$ is the correction matrix from Eq. 20, see [31].

Furthermore, the equation of motion is extended by the correction schemes artificial viscosity following [29] and artificial stress presented by [22] to stabilize the simulation.

Various methods have been published for the treatment of the solid wall boundary conditions, such as adding fictitious particles, repulsive force functions and boundary integrals to enforce impermeability [35]. Repulsive forces are beneficial compared to the other methods for complex geometries defined by triangular meshes like the drill geometries used in this investigation. Therefore, the interaction between the SPH fluid particles and the solid wall boundaries is modeled by a modified Lennard-Jones potential as presented in [24]. This repulsive force is defined as normal to the surface of each triangle. It is calculated as

$$F_d = \begin{cases} \psi \frac{(R-d)^4 - (R-s)^2(R-d)^2}{R^2 s(2R-s)} & \text{if } d \le R, \\ 0 & \text{otherwise,} \end{cases} \tag{24}$$

where R is the maximum range for interaction and d is the absolute distance between the contact particle and the triangle. The scalar ψ controls the stiffness of the interaction and describes the maximum force at zero distance. Unlike the original Lennard-Jones potential, it does not tend to infinity. The distance for which the resulting force switches from repulsive to attractive is denoted by parameter s. For the simulations, the parameter s equals the maximum interaction range R, resulting in repulsion only. A reasonable choice for the stiffness parameter ψ is given in [15], which proposes that an SPH particle with the maximum velocity occurring during the simulation is stopped only by the conservative normal forces at, e.g. half ($q = 0.5$) of the modified Lennard-Jones potential interaction range. Based on this assumption,

$$E_{\mathrm{kin}} = \frac{1}{2} m v_{\max}^2 \stackrel{!}{=} \int_q^1 F_{\mathrm{d}}(q) \mathrm{d}q \mid_{q=d/R} = E_{\mathrm{pot}}(q), \quad (25)$$

can be estimated, neglecting gravitational forces, which are small compared to repulsive forces.

Table 1 Boundary conditions and SPH parameters

Property	Symbol	Value	Unit
Drill diameter	D	30	mm
Fluid density	ρ	999	$\mathrm{kg} \cdot \mathrm{m}^{-3}$
Dynamic viscosity	μ	1e-2	$\mathrm{kg} \cdot \mathrm{m}^{-1}\mathrm{s}^{-1}$
Inflow velocity	v	5.0	$\mathrm{m} \cdot \mathrm{s}^{-1}$
Angular velocity	ω	66.7	$\mathrm{rad} \cdot \mathrm{s}^{-1}$
Artificial viscosity factors	α	0.05	
[29]	β	0.1	
Artificial stress factor [22]		0.2	
Diffuse density factor	δ	0.1	
Artificial speed of sound	c_0	50	$\mathrm{m} \cdot \mathrm{s}^{-1}$
CFL		0.1	
Initial particle distance	Δ	3.5e−4	m
Smoothing length	h	5.25e−4	m
Simulation hardware	AMD Ryzen 9 5950X		
Simulation time	T	10	days
Number of particles	n_p	≈ 275,000	

3.2 Simulation model

Having presented the essential numerical fundamentals of the particle method, SPH is used to simulate the cutting fluid flow at the head of the ejector drill. Starting from the reference simulation, where the experimental setup is simulated for validation, the rotation of the drill is added to the simulation model, and four different design modifications of the drill head are modeled. The simulations start from an initially empty borehole with a constant cooling liquid inflow close to the drill head until a nearly steady state is reached. The inflow is placed after the MWF outlet bores and assumed as laminar flow with a velocity of $5\,\mathrm{m} \cdot \mathrm{s}^{-1}$ based on experimental data obtained through high-speed recording using particle image velocimetry (PIV) [13], as mentioned earlier. It is modeled to rotate identically to the rotation of the tool as the fluid flows through an arrangement of MWF outlet bores, which rotate too, before reaching the drill head. In the experiments for the PIV analysis, water is used for the better visibility of the added tracer particles instead of the opaque MWF. For the further investigation, a mixture of about ten percent concentrated metal working fluid and water is used, as in the real production process. Homogeneous properties are assumed based on the convex combination of their individual properties according to the mixing ratio. The resulting higher viscosity compared to the PIV experiments is presumed to decrease the vortex formation. A comparative simulation is therefore carried out to investigate this in more detail. Furthermore, isotherm conditions are assumed for the simulation model. This follows the experiments, where the heating of the MWF is negligible for the investigated period as a 1,000 liter reservoir of MWF with a temperature of 20 °C is used. Table 1 lists the applied boundary conditions and SPH parameters for the simulations.

Figure 5 shows the investigated drill head design modifications next to the reference drill head. The view is fixed on the outer cutting edge. The modifications I, II and III target a decrease in the flow area at the cutting edge by an adaption of the outer tool wall, thereby increasing the cover of the chip mouth to reduce the vortex at the cutting edge. In contrast, modification IV removes the outer tool wall to increase the flow area at the cutting edge to achieve an improved chip evacuation.

The chip evacuation is not modeled in the simulations as the influence of these modifications on the vortex generation are examined as a preparatory action. Based on the simulation results, selected modifications will be investigated with the chip evacuation explicitly modeled in future investigations.

Compared to the experiments, the rotation of the tool is neglected for the first simulation of the reference design. The tool rotation is considered for the second simulation of the reference design and simulations of the modified designs.

The inflow constantly adds fluid particles to the simulation, and the outflow, placed in the inner tube, removes the particles from the simulation domain. Thereby, the required computational effort is reduced compared to a constant particle setup. About 275,000 particles are used in the simulation domain at the end of the presented results. The simulations take about 10 days on AMD 5950X machines using 14 cores. Additional parts, such as the indexable inserts and guide pads, are added to the simulation models despite not being shown in Fig. 5.

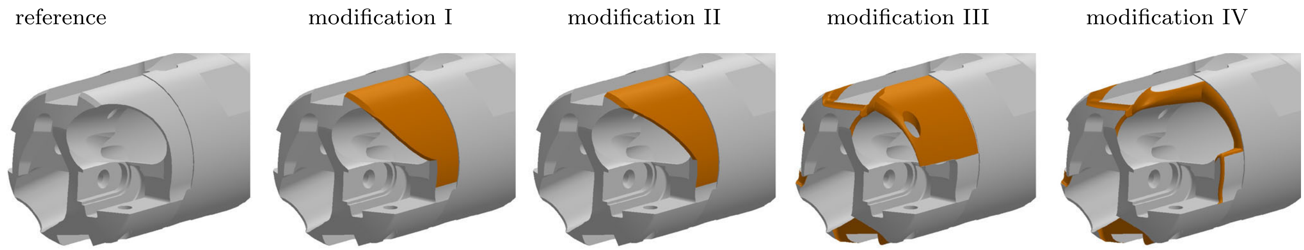

Fig. 5 Reference drill head and the modified designs with the changes to the chip mouth highlighted

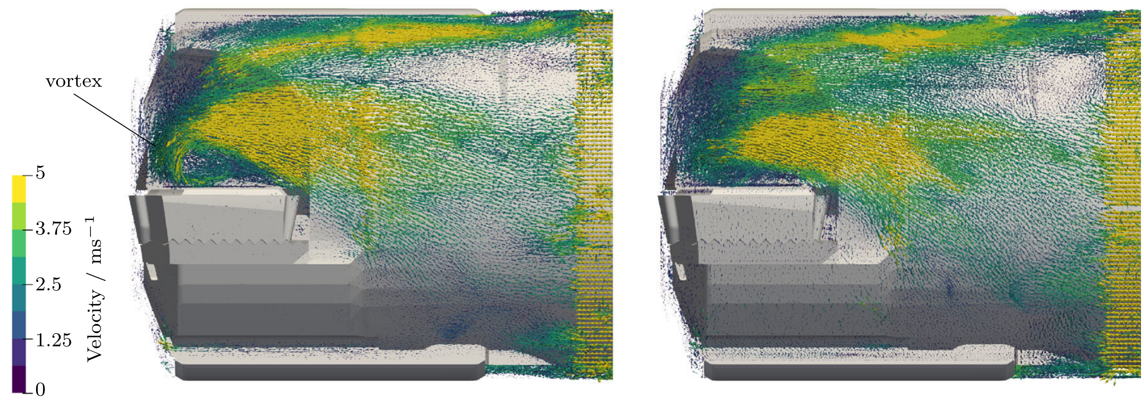

Fig. 6 Fluid flow for the reference drill without rotation of the drill (left) and with a rotation of $\omega = 66.7\,\mathrm{s}^{-1}$ (right)

The coolant pump creates a high fluid pressure at the inflow of the simulation domain, while in the inner tube an underpressure occurs at the outflow created by the ejector nozzles. However, the WCSPH approach used in this investigation cannot handle these special pressure conditions for the open boundaries. Instead, only a velocity boundary condition is applied to the influx. The impossibility of applying Dirichlet boundary conditions on the pressure at the open boundary limits the correct evaluation of the pressure within the flow. Furthermore, the WCSPH approach does not allow the exact evaluation of pressure fields in the fluid due to the spurious numerical oscillations. Therefore, the ejector effect and the resulting influence on the pressure distribution cannot be modeled correctly by WCSPH. However, the additional underpressure in the inner tube is expected to improve the flow. Therefore, this modeling can be considered a conservative assumption, allowing a better understanding of the flow resistance of the investigated design modifications. The incompressible SPH approach (ISPH) overcomes such difficulties but creates other challenges.

4 Results

Figure 6 shows the fluid flow at the drill head for the reference tool without drill rotation (left side) and with drill rotation (right side) after the fluid flow is nearly static. The inflow is located on the right side, and arrow glyphs visualize the flow, which are sized by the velocity magnitude of the flow. The view is centered on the outer cutting edges, and two streams can be observed from the inflow to the front. The primary stream flows along the outer cutting edge into the chip mouth of the drill. A secondary stream can be identified flowing around the guide pads and is located in the upper half of the image. The general flow characteristics and the quantitative values agree with the experimental results in Sect. 2. The fluid flows with a medium velocity at the right end of the drill head and is accelerated as it flows around the cutting edges through the chip mouth opening. The characteristic vortex identified in the experiments can also be seen in the primary stream for the reference tool without drill rotation. The earlier stated influence of the fluids viscosity on the vortex formation cannot be seen. The influence therefore does not appear to be of a decisive magnitude. The vortex is still visible after adding the tool's rotation into the modeling. However, its intensity is already decreased compared to the simulation results without drill rotation. The general flow behavior is similar for both simulations of the reference drill head design, with and without drill rotation. The same has to be expected for the experiments as the tool is also kept static to allow the video camera to observe the cutting process. The boreground and the see-through borehole are rotated instead. Consequently, a decrease of the vortex is likely for the real-world application where the drill rotates.

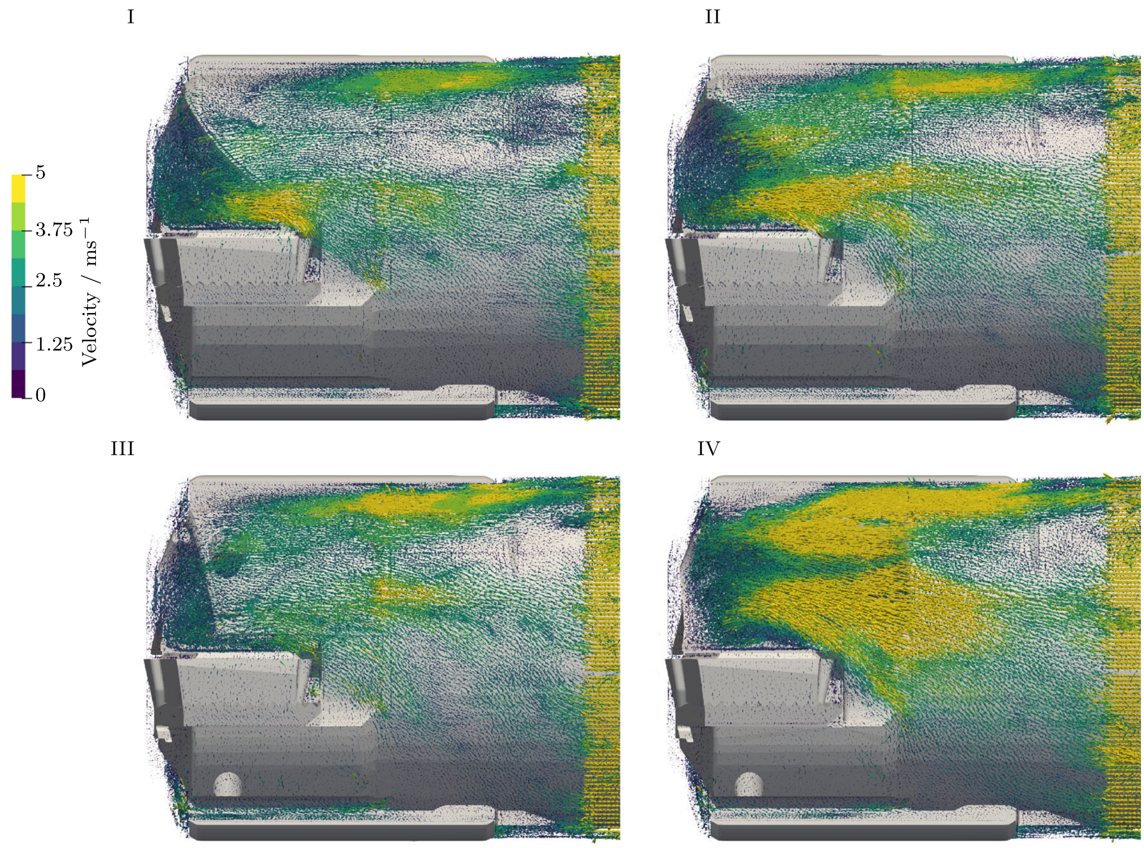

Fig. 7 Fluid flow at the drill head for the different drill design modifications

Figure 7 shows the fluid flow for the drill head modifications in the chip mouth opening design. The general flow characteristics of two major streams from the inflow to the front can also be observed for all modifications. However, the individual streams are different compared to the reference simulations. All modifications are modeled with a rotating tool. Thus, the vortex has already decreased compared to the non-rotating tool, as the comparison of the reference simulations shows. Modification I, which extends the cover in a parabolic arc over the chip mouth, disrupts the secondary stream almost completely. However, it pushes the primary stream closer to the outer cutting edge and prevents the vortex from forming. In contrast, the second modification design (II), a linear closing of the chip mouth, does not cause such a strong decrease in the secondary stream. Moreover, the variant also prevents forming the vortex in the primary stream. A design variant, which closes the chip mouth almost entirely up to the drill front, is investigated as modification design III. A small hole in the cover is added near the guiding pad to allow some fluid flow in the area of the secondary stream. However, both streams are significantly decreased by the introduced modification, especially since the primary flow is almost completely disrupted, preventing the vortex formation. The chip mouth is completely opened in the last modification design (IV). This leads to an increase in the width of both streams. However, the fluid flow is significantly slowed down before reaching the front of the drill head and the majority flows earlier inside the drill head and back through the inner tube. Furthermore, the flow is similar to the reference design, exhibiting the same flow features, including forming a small vortex near the outer cutting edge.

The general flow analysis of the simulation results shows that some design modifications can prevent the vortex formation. However, according to the flow visualization, some designs affect the general flow significantly. Therefore, additional flow meters are placed at the drill head to measure how much fluid volume flows through each section. This allows the analysis, if the design modifications reduce the flow volume or lead to a relocation of the flow along the cutting edge to other parts of the drill. The drill head can be clustered into two sections, depending on through which opening the MWF flows inside the drill head.

Figure 8 shows the location of the flow meters. The cross section considered for the flow meter measuring the flow through the cutting edge region is colored orange in the figure, and the other region is colored blue. Figure 9 plots the total net flow rate summing up both sections of the drill head. The flow rate data is smoothed by a simple moving average

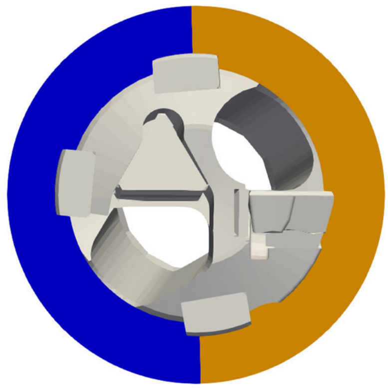

Fig. 8 Visualization of the flow meter cross sections: The area of the cutting edge section is colored orange, and the cross section of the other regions at the drill head front is colored blue. (Color figure online)

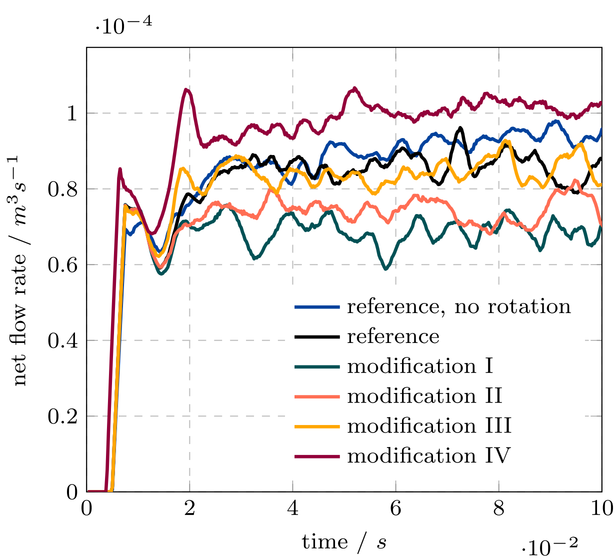

Fig. 9 Total net flow rate at the drill head for the different design modifications

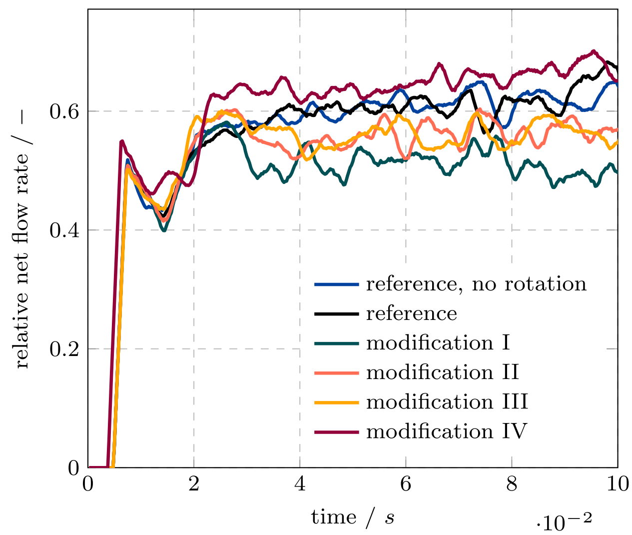

Fig. 10 Net flow rate in the cutting edge section relative to the net total flow rate at the drill head

with a window size of 2.5 ms to remove the noise from the explicit integration. Any backflow from the cutting head back through the flow meter cross section is subtracted from the flow rate to obtain only the net flow rate through each section, which flows subsequently through the inner of the drill. The inflow starts at $t = 0$ s and reaches the flow meters with a small delay. Afterward, the fluid flows unrestricted until it hits the bore ground, and the flow rate decreases as the fluid volume increases resistance for the following fluid. This causes an increase in the pressure, and the flow rate increases and stabilizes over time until it reaches a steady state.

The flow rate for the reference design is similar for both cases, with and without the tool's rotation. The data suggests that without rotation, the flow resistance is smaller. However, the difference between both is negligible. Design modification I shows the lowest flow rate of the investigated designs, whereas modification IV exceeds the flow rate of the reference design. Design modifications II and III show a similar flow rate to the reference design. However, the flow rate for modification II is smaller than for the reference design but still higher than design modification I.

Figure 10 shows the net flow rate at cutting edge relative to the total net flow rate at the drill head. It shows the same behavior in the beginning as the total net flow shown in Fig. 9. However, it allows the analysis of the amount of fluid flowing through the cutting edge section compared to the other sections. Compared to the reference design, modification IV allows a larger proportion of the MWF to flow through the cutting edge section, whereas modification II, III and IV are similar to the reference design or a bit worse.

It can be seen that the additional covering of the chip mouth of the modifications (I, II, III) reduces the vortex generation as the flow is channeled but leads to an increased flow resistance with an increased covering. An increased flow resistance and the reduced flow rate can cause problems in the chip evacuation or can lead to a reduced cooling and lubrication of the cutting edges, reducing the tool's lifetime. Design modification III partially contradicts this observation with its almost complete cover of the chip mouth. However, according to the fluid flow visualization, this is caused mainly by an additional hole in the chip mouth covering. This would allow reliable chip removal. Nonetheless, the reduced flow at the cutting edge decreases the cooling and lubrication. Consequently, a moderate covering like the modification I or II is a good balance.

In contrast to the other modifications, completely removing the chip mouth covering increases the flow rate through the cutting edge section. However, the flow visualization shows that the vortex generation is not decreased. Furthermore, the flow is significantly slowed down before reaching the front of the drill head and the majority of the fluid flows earlier inside the drill head and back through the inner tube. This could lead to a decreased cooling and lubrication of the cutting edges despite an increased total net flow.

5 Conclusions

Experimental investigations of ejector deep hole drilling show a vortex formation at the outer cutting edge. This vortex can lead to a delayed chip removal from the cutting zone as small chips can be caught in the vortex. In consequence, the removal of chips is slower than they are produced, and this can lead to chip clogging, and might result in drill breakage due to an increased torque. The experiments were conducted using a see-through test sample and non-rotating tool to allow the observation of the metalworking fluid flow using a high-speed camera. Additionally, polyamide particles were added to the flow to visualize the flow using particle image velocimetry. To mitigate the vortex formation, different design modifications of the chip mouth covering were investigated. To eliminate the need for expensive prototype production and reduce the number of experiments, simulations were used. Therefore, the SPH method was applied. SPH allows the prediction of the fluid movements using the Navier–Stokes equations especially for moving surfaces and interfaces, which are dominant in the modeling of the ejector deep hole drilling process.

The simulation of the reference design used in the experiments shows good agreement with the particle image velocimetry results, including the vortex formation. By adding the tool's rotation, which is not included in the experiments for observation reasons, the vortex formation is already slightly reduced. However, the additional covering of the chip mouth in some of the modifications (I, II, III) is able to reduce the vortex formation beyond this level as the flow is channeled. Nevertheless, this causes an increased flow resistance with increased covering. An increased flow resistance and the reduced flow rate can cause problems in the chip evacuation or lead to a reduced cooling and lubrication of the cutting edges, reducing the tool's lifetime. The investigated design modifications I and II show a good balance between reducing the vortex formation and maintaining a sufficient fluid flow along the cutting edges.

In contrast to an increased covering of the chip mouth, a complete removal of the chip mouth has the advantage that it leads to an increased flow rate along the cutting edges. However, the flow exhibits the same flow characteristics as the reference design including the vortex formation. Furthermore, the chip mouth removal leads to early entrance of the flow into the inner tube, which could prevent a sufficient cooling and lubrication of the cutting edges.

Future work will include the modeling of the chip evacuation to estimate the influence of the changed flow due to the modifications. Furthermore, experimental studies of some of the design modifications are planned to validate the simulation results and to include the ejector effect in the inner tube which was not modeled in the simulations. Finally, further research into the modeling of the ejector effect and the underpressure in the inner tube will be carried out.

Acknowledgements This research was supported by the Deutsche Forschungsgemeinschaft (DFG) under grant numbers 439917965 and 405605200.

Funding Open Access funding enabled and organized by Projekt DEAL.

Declarations

Conflict of interest The authors declare that they have no conflict of interest.

References

1. Antuono M, Colagrossi A, Marrone S, Diego M (2010) Free surface flows solved by means of SPH schemes with numerical diffusive terms. Comp Phys Comm 181:532–549
2. Astakhov VP, Subramanya PS, Osman MOM (1995) Theoretical and experimental investigations of coolant flow in inlet channels of the BTA and ejector drills. Proc Inst Mech Eng Part B 209(3):211–220
3. Astakhov VP, Subramanya PS, Osman MOM (1996) On the design of ejectors for deep hole machining. Int J Mach Tools Manuf 36(2):155–171
4. Baumann A, Oezkaya E, Schnabel D, Biermann D, Eberhard P (2021) Cutting-fluid flow with chip evacuation during deep-hole drilling with twist drills. Eur J Mech B/Fluids 89:473–484
5. Baumann A, Oezkaya E, Biermann D, Eberhard P (2022) Geometry modifications of single-lip drills to improve cutting fluid flow. Adv Manuf Technol Int J Adv Manuf Technol 121:1689–1695
6. Biermann D, Bleicher F, Heisel U, Klocke F, Möhring H-C, Shih A (2018) Deep hole drilling. CIRP Annals 67(2):673–694
7. Bonet J, Lok T-SL (1999) Variational and momentum preservation aspects of Smooth Particle Hydrodynamic formulations. Comput Methods Appl Mech Eng 180:97–115
8. Chin J-H, Hsieh C-T, Lee L-W (1996) The shaft behavior of BTA deep hole drilling tool. Int J Mech Sci 38(5):461–482

9. Cole RH (1948) Underwater explosions. Dover Publications
10. Chu N-H, Nguyen D-B, Ngo N-K, Nguyen V-D, Tran M-D, Vu N-P, Ngo Q-H, Tran T-H (2018) A new approach to modelling the drilling torque in conventional and ultrasonic assisted deep-hole drilling processes. Appl Sci 8(12):1–12
11. Fritsching U, Buss L, Tonn T, Schumski L, Gakovi J, Hatscher JD, Sölter J, Avila K, Karpuschewski B, Gerken JF, Wolf T, Biermann D, Menze C, Möhring H-C, Tchoupe E, Heidemanns L, Herrig T, Klink A, Nabbout K, Sommerfeld M, Luther F, Schaarschmidt I, Schubert A, Richter M (2023) Flow visualisation and evaluation studies on metalworking fluid applications in manufacturing processes-methods and results. Processes 11(9):2690
12. Furness RJ, Galip Ulsoy A, Wu CL (1996) Feed, speed, and torque controllers for drilling. ASME J Eng Ind 118(1):2–9
13. Gerken JF, Canini D, Biermann D, Eberhard P (2022) Scientific investigation of the cooling lubricant flow in ejector deep hole drilling inside the tool using innovative analysis methods. In: Proceedings 16th CIRP Conference on Intelligent Computation in Manufacturing Engineering, CIRP ICME ’22, 2022
14. Gerken JF, Canini D, Biermann D, Eberhard P (2023) Design of fluid flow optimized ejector drill heads for efficient metalworking fluid supply to the cutting zone. Procedia CIRP 119:351–356
15. Kazaz L (2016) Investigation of lubricant efficiency losses in gearboxes by FSI using co-simulation between GTM and Pasimodo (in German). Thesis MSC-247, Institute of Engineering and Computational Mechanics, University of Stuttgart
16. Kumar MS, Deivanathan R (2021) Effect of process parameters on drilling–an overview. Mat Today Proc 46(2):1401–1406
17. Liu MB, Liu GR (2010) Smoothed particle hydrodynamics (SPH): an overview and recent developments. Arch Comput Methods Eng 17(1):25–76
18. McLean D (2012) Understanding aerodynamics: arguing from the real physics. Wiley
19. Mellinger JC, Ozdoganlar OB, DeVor RE, Kapoor SG (2002) Modeling chip-evacuation forces and prediction of chip-clogging in drilling. J Manuf Sci Eng 124(3):605–614
20. Mellinger JC, Ozdoganlar OB, DeVor RE, Kapoor SG (2003) Modeling chip-evacuation forces in drilling for various flute geometries. J Manuf Sci Eng 125(3):405–415
21. Monaghan JJ (1994) Simulating free surface flows with SPH. J Comput Phys 110(2):399–409
22. Monaghan JJ (2000) SPH without a tensile instability. J Comput Phys 159(2):290–311
23. Monaghan JJ, Kos A, Issa N (2003) Fluid motion generated by impact. J Waterw Port Coast Ocean Eng 129(6):243–300
24. Müller M, Schirm S, Teschner M, Heidelberger B, Gross M (2004) Interaction of fluids with deformable solids. Comput Anim Virtual Worlds 15(3–4):159-171
25. Mueller A (2017) Dynamic refinement and coarsening for the smoothed particle hydrodynamics method. dissertation, Schriften aus dem Institut fuer Technische und Numerische Mechanik der Universitaet Stuttgart, Volume 46, Aachen, Germany
26. Nagao T, Hatamura Y, Mitsuishi M (1994) In-process prediction and prevention of the breakage of small diameter drills based on theoretical analysis. CIRP Annals 43(1):85–88
27. Oezkaya E, Baumann A, Michel S, Schnabel D, Eberhard P, Biermann D (2023) Cutting fluid behavior under consideration of chip formation during micro single-lip deep hole drilling of Inconel 718. Int J Model Stimul 43(2):49–63
28. Oezkaya E, Baumann A, Eberhard P, Biermann D (2022) Analysis of the cutting fluid behavior with a modified micro single-lip deep hole drilling tool. CIRP-JMST 38:93–104
29. Price DJ (2012) Smoothed particle hydrodynamics and magnetohydrodynamics. J Comput Phys 231(3):759–794
30. Raffel M, Willert CE, Scarano F, Kähler CJ, Wereley ST, Kompenhans J (2018) Post-processing of PIV Data. In: Particle Image Velocimetry, Springer, Cham, 2018
31. Randles PW, Libersky LD (1996) Smoothed particle hydrodynamics: some recent improvements and applications. Comput Methods Appl Mech Eng 139:375–408
32. Richardson R, Bhatti R (2001) A review of research into the role of guide pads in BTA deep-hole machining. J Mater Process Technol 110(1):61–69
33. Shadloo MS, Yildiz M (2011) Numerical modeling of Kelvin-Helmholtz instability using smoothed particle hydrodynamics. Int J Numer Methods Eng 87(10):988–1006
34. Sollich D, Reinheimer RN, Wagner J, Berger P, Eberhard P (2022) An improved recoil pressure boundary condition for the simulation of deep penetration laser beam welding using the SPH method. Eur J Mech B/Flu 96:26–38
35. Violeau D, Rogers BD (2016) Smoothed Particle Hydrodynamics (SPH) for free-surface flows: past, present and future. J Hydraul Res 54(1):1–26
36. Wendland H (1995) Piecewise polynomial, positive definite and compactly supported radial functions of minimal degree. Adv Comput Math 4:389–396